# An oxide-based flexible electrochromic transistor under mechanical stress

Takaki Onozato[1*], Hai Jun Cho[1,2], and Hiromichi Ohta[1,2*]

[1]*Graduate School of Information Science and Technology, Hokkaido University, N14W9, Kita, Sapporo 060−0814, Japan*

[2]*Research Institute for Electronic Science, Hokkaido University, N20W10, Kita, Sapporo 001−0020, Japan*

E-mail: takaki_onozato6@eis.hokudai.ac.jp, hiromichi.ohta@es.hokudai.ac.jp

**Today mechanical flexibility has become an important feature for electronic devices, especially in flat display panels. Here we demonstrate the device operation of a tungsten oxide based flexible electrochromic transistor (ECT), which was fabricated on 0.1-mm-thick polyethylene terephthalate film. The ECT can be operated by applying voltage of ±3 V for 1 s when the radius of curvature was larger than 16 mm, indicating that the flexible ECT exhibited a strong resistance to static strains. However, the resistance of the channel increased by fatigues from applying cyclic flexural strains. Present flexible ECT would highly be useful for the economically viable curved display panels. However, its vulnerability to fatigue needs improvements for other applications.**

## 1. Introduction

Mechanical flexibility has become an important feature for electronic devices as the elimination of mechanical constraints is essential for various applications including modern flat display panels (FPDs), solar cells, and sensors. Therefore, flexible electronics research area is rapidly growing[1)]. Experimentally demonstrated examples include: flexible-circuits[2)], thin film transistors (TFTs)[3)], organic light emitting diodes (OLEDs)[4)], tensor sensors[5)], and solar cells[6),7)]. In this study, we focus on adding flexibility in electrochromic transistors (ECTs), which can be utilized to simultaneously store both optical and electronic states [8),9)].

Like TFTs, ECTs are composed of three electrodes of source, drain, and gate. However, their operation mechanism is different from that of conventional TFTs. In order to turn on/off the ECT, electrochemical redox reaction is utilized whereas pure electrostatic charge accumulation/depletion is utilized in TFTs. Similar to an electrochromic display (ECD)[10-12)], the color of ECT can be modulated simultaneously with increase/decrease of the electrical resistivity. This is due to the changes in the valence state of the transition metal ion in the active material, which can be changed by the electrochemical redox reaction. Since the electrochemical redox reaction switches the chemical composition of the active material, ECTs attributes as a non-volatile memory. In addition, the energy consumption is significantly low as compared to other FPDs such as liquid crystal displays (LCDs) and OLEDs.

ECT (ECD) is composed of electrolyte/active material laminate, which is sandwiched by two electrodes. Previously, liquid electrolytes[13-15)] were used as the electrolyte of ECT. Therefore, previous ECTs were highly vulnerable to mechanical failures that can be caused by bending. In order to overcome this problem, recent studies successfully demonstrated the operation of all-solid-state ECTs[9,16-18)], which were fabricated at room temperature. Although the room temperature fabrication is compatible with economically viable flexible materials, all-solid-state ECTs on flexible substrates have not been demonstrated yet.

The all-solid-state ECT device consists of four different oxide layers including electrochromic amorphous $WO_3$, water moisture containing $TaO_x$ as porous gate insulator,

shunting ZnO layer, and transparent conducting ITO electrodes.[16] The mechanical properties of oxides tend to be brittle. Therefore, if these materials are deposited on flexible substrates as a device, clarifying the effect of mechanical strains on the device performance is crucial for understanding the physical flexural limitations as well as improving the flexibility.

Here we demonstrate the operation of all-solid-state ECTs on flexible substrates and investigate the effect of static/cyclic flexural strains on the device performance. The flexible ECT without any strain showed excellent performances including fast operation within 1 s at low operation voltage of ±3 V just like ECTs on rigid substrates[16]. The device showed strong resistant to static strains. However, its performance was highly vulnerable to cyclic stresses, which is typical mechanical characteristic of oxides. This work suggests that the present flexible ECT has a great potential for curved display panels, and the flexural strain test results will be of great value in understanding the flexural durability of layer structured devices consist of oxide films.

## 2. Experimental methods

The flexible ECT device was fabricated on 100-μm-thick polyethylene terephthalate (PET) substrate (Nakai Industrial Ltd., 20 × 20 × 0.1 mm). The oxide thin films were deposited by pulsed laser deposition (PLD, KrF excimer laser) at room temperature with different stencil masks. Two differently sized devices were prepared. The channel length ($L$) × channel width ($W$) of the ECT were 100 μm × 200 μm and 800 μm × 400 μm, respectively. First, 30-nm-thick polycrystalline ZnO film was deposited on a PET film as the bottom TCO layer, which applies a uniform electric field in the active layer and increases the operating speed[16]. Then 60nm-thick ITO/ZnO films were deposited as transparent electrodes (source and drain). Next, 100-nm-thick amorphous $WO_3$ active layer[19], 250-nm-thick tantalum oxide ($TaO_x$) solid-electrolyte layer[20], and 20-nm-thick polycrystalline NiO layer were deposited sequentially on the bottom TCO layer. The NiO plays as a counter layer ($NiO + OH^- \rightarrow NiOOH + e^-$)[21]. Finally, 60-nm-thick ITO/ZnO bilayer film was deposited as the transparent gate electrode on the NiO layer. **Figure 1** shows the optical micrograph and schematic cross-sectional view of the resultant flexible ECT, which was bendable.

## 3. Results and discussion

### 3.1 Results

#### 3.1.1 Optical transmission

In order to check the electrochromism of the resultant flexible ECT, we measured the optical transmission spectra by UV-VIS Fiber-microscope (Source: L7893, HAMAMATSU Co., Detector: HR4000 High-Resolution Spectrometer, Ocean Optics Inc.). For protonation, we applied a gate voltage ($V_g$) of +3 V for 3 s to the flexible ECT. The as-prepared ECT was almost colorless and transparent , but it changed to dark blue upon protonation, which is similar to our previously reported ECT on rigid substrates.[16] The optical transmission in the visible light region (400−800 nm in wavelength) drastically decreased to 28 % after protonation. However, upon de-protonation ($V_g$ = −3 V for 3 s), the transmission recovered to 71 % in the visible region as shown in **Fig. 2**. The inset shows the optical micrograph of the protonated and de-protonated device, which clearly demonstrates the electrochromism of the resultant flexible ECT.

#### 3.1.2 Effect of static flexural strain

Then we examined the effect of bending on the electron transport of the ECT during protonation and de-protonation using 800 μm ×400 μm sized devices. We bent the resultant ECT at fixed radii of curvature (30 mm, 16 mm, 12 mm, and 6 mm) and performed protonated / de-protonated the device. **Figure 3(a)** shows the optical micrograph of the experimental setups of the bending test of the ECT devices at various radii of curvature. The tensile strain on the films was estimated with the ratio between half the substrate thickness and the radius of curvature ($r$)[22], which yields 0.16 % for 30 mm, 0.31 % for 16 mm, 0.41 % for 12 mm, and 0.83 % for 6 mm. **Figure 3(b) shows** the sheet conductance ($\sigma_s$) as a function of operating gate voltage $\pm V_g$ at each radius of curvature. First, a positive gate voltage ($V_g$) from +0.5 V to +5 V was applied to protonate the device (**Fig. 3b** left panel, each $V_g$ application time of 1s), and then negative $V_g$ also applied from -0.5 V to −5 V to de-protonate the device (**Fig. 3b** right panel, each $V_g$ application time of 1 s). The $\sigma_s$ values were measured by the dc four-probe method with van der Pauw electrode configuration with a source measure unit (Keithley 2450). The detail of our electrical conductivity measurement was

described elsewhere.[9,16] The initial $\sigma_s$ (~$10^{-4}$ $\Omega^{-1}$ sq) reflects the $\sigma_s$ of the 30 nm ZnO thin film (bottom TCO layer). In case of curvature radius ($r$) = flat, 12 mm and 16 mm, the $\sigma_s$ gradually increase then suddenly reach to ~$10^{-2}$ $\Omega^{-1}$ sq at +3 V. On the other hand, in the case of $r$ = 12 mm and 6 mm, $V_g$ = +3.5 V and 4 V were required for $\sigma_s$ to reach ~$10^{-2}$ $\Omega^{-1}$ sq, respectively. Subsequently, by applying negative $V_g$, $\sigma_s$ clearly recovered, reaching the initial state at $V_g$ = −3.5V. **Figure 3(c)** summarizes the retention-time ($t$) dependence of the $R_s$ at various radii of curvature. We measured the sheet resistance ($R_s$) every 1 s after the protonation / de-protonation at room temperature. For protonation, positive d.c. gate voltage (+3 V) was applied to the ECT for 1 s, and then the $R_S$ was measured. This sequence was repeated several times. Similarly, for de-protonation, negative d.c. gate voltage (−3 V) was applied to the ECT for 1 s, and then $R_S$ was measured. This sequence was repeated several times as well. The solid lines are the results of the logistic function fitting. When $r$ was larger than 16 mm, the relationship between $R_s$ and retention time ($t$) did not change significantly; the $R_s$ decreased from ~4000 Ω $sq^{-1}$ to ~100 Ω $sq^{-1}$ within 1 s during protonation and increased from ~100 Ω $sq^{-1}$ to ~4000 Ω $sq^{-1}$ within 1 s during de-protonation. However, $R_s$ started to increase when the $r$ was below 16 mm, and the operating time increased slightly from < 1 s to 2−3 s.

Overall, flexural strains increased the operation voltage and operation time of the flexible ECTs, and the protonation stages were affected a bit more strongly. Surprisingly, despite the changes in the operation time, the absolute values of $R_s$ after protonation/deprotonation were not significantly affected by the static flexural strains. This suggests that the active $WO_3$ and shunting ZnO remain unharmed up to $r$ = 6 mm. On the other hand, the resistance of the top gate electrode before the bending experiment was ~ 100 Ω, but it increased to ~ 10 kΩ, after the bending test at radius $r$ = 6 mm. This indicates the operation delay due to the flexural strains is mainly attributed to mechanical damages in the ITO/ZnO electrodes (gate). This is likely attributed to the fact that the outermost layer is under the highest tensile strain. Therefore, the static flexure strain degrades the operation speed, but overall, the present flexible ECTs show great performance which 3V, 1sec operation in $r$ > 16 mm. These results indicate that present ECTs are resistant to static flexural strains and have the potential for curved display applications.

Finally, we tested the effect of cyclic flexural strains on the flexible ECT device performance. We repeatedly exerted bending moments (i.e. minimum strain = 0, maximum strain ≠ 0) to the flexible ECTs, and the bending axis was parallel to the long axis of the device. 800 μm × 400 μm sized device worked only for 50 flexural cycles even under at $r$= 16 mm. Since resistance to cracking increases with decreasing size [23], we performed the cyclic tests using 200 μm × 100 μm sized device. We bent the ECT 10 times, then performed protonation / de-protonation. After each protonation / de-protonation, we measured the two-terminal resistance. Since the 200 μm × 100 μm size device only has a two-terminal source-drain electrode, two-terminal resistance($R$) and sheet resistance ($R_S$) can be compared by $R_S = R(W/L)$. The test was performed until the device showed infinite resistance, which indicates a complete mechanical failure in the device (or fatigue limit). **Figure 4** shows the changes in the two-terminal resistance ($R_{\text{deprotonation}}$, $R_{\text{protonation}}$) as a function of flexural cycles at various $r$ ($r$ = 16, 12 and 6 mm). At $r$ = 16, 12, and 6 mm, the device lasted ~410, ~220, and ~30 cycles, respectively. Before the test, the ECT showed $R_{\text{deprotonation}}$ ~35 kΩ and $R_{\text{protonation}}$ ~1 kΩ. Both $R_{\text{deprotonation}}$ and $R_{\text{protonation}}$ gradually increased with the number of cycles.

## 3.2 Discussion

In general, cyclic flexural strains have a significant effect on the device compared to static flexural strains. During the cyclic flexural strains test, the resistance values of the active $WO_3$ layer and ZnO layer, which are directly related to protonated and de-protonated states, gradually increased in all cases. This suggests that both the active $WO_3$ and shunting ZnO are being affected by the cyclic flexural strains, which is drastically different from the effect of static flexural strains. This is not surprising since most materials show higher strengths in static strain tests[23]. These results show that the present ECTs are highly susceptible to fatigue and not suitable for applications that require dynamic strain resistant unless the radius of curvature is large.

Furthermore, we observed the optical micrographs of the device after bending tests by Laser scanning microscope (VK-9710, KEYENCE). The optical micrographs of the fractured devices at their fatigue limits after cyclic flexural strains are shown in **Fig. 5(a), (b), and (c)**,

the radii is $r$ = 16, 12 and 6 mm, respectively. At all radii, the cracks in the device resemble mode I fracture, where the crack propagation direction and the fracture surface are perpendicular to the tensile stress. Above $r$ = 12 mm, a series of straight crack lines are observed, which are typical brittle fracture characteristics commonly observed form amorphous oxide films[24-27]. This strongly suggests that the crack initiates in the outer ITO top gate electrode, which is consistent with the device performance tests. However, at $r$ = 6 mm, the long crack lines become short elliptical pores that are clustered. This suggests a change in the fracture mechanism when $r$ decreases from 12 mm to 6 mm. The new failure mechanism is likely attributed to the fracture of porous $TaO_x$ since short elliptical pores come from the evolution of micropores[23]. This cracking mechanism is likely related to the sharp performance degradation during the cyclic flexural stress tests at $r$ = 6 mm as well as the large device (800 μm ×400 μm, only lasted 50 cycles) since these cracks are initiated at the micropores and the 200 μm × 100 μm sized device exhibits less number of pores. Compared to failures in ITO, mechanical damages in $TaO_x$ is much more critical to the device performance since the active $WO_3$ is directly in contact with the $TaO_x$. The fracture characteristics demonstrate that the flexure strengths of ETCs are limited by the ITO electrode and $TaO_x$ at low and high tensile strains, respectively.

The present flexible ECTs exhibited good resistance to static flexural strains, and the corresponding performance degradation is a minor delay in the device operation with no damages in the $WO_3$ and ZnO layers. Since the main damage in the device structure is in the ITO/ZnO electrodes, changing the gate electrode to flexible materials[28] or fabricating special structure[29-32] would improve the device performance under static flexural strains. In contrast, fatigue from cyclic flexural strains noticeably degraded the electrical properties of $WO_3$ and ZnO, which decreased the ECT performance. The fatigue limit drastically decreases if $r$ changes from 12 mm to 6 mm, and $r$ > 16 mm seems to be necessary to maintain reasonable device performance under cyclic flexure stresses. Adding another layer that exerts compressive strains on the device can potentially negate the tensile strains from bending, but detailed failure analysis in the future is necessary to improve the cyclic flexural durability of the present device.

## 4. Conclusions

In summary, we demonstrated the performance of a flexible ETC on 0.1-mm-thick polyethylene terephthalate substrate, which was fabricated using pulsed laser deposition technique at room temperature. The ETC consists of electrochromic tungsten oxide, water containing porous gate insulator tantalum oxide, and transparent conducting ITO. The resultant ECTs showed fast operation within 1 s at low operation voltage of ±3 V while showing excellent resistance to static flexural strains. However, their performances were strongly degraded by cyclic flexural stresses and fatigues, which were evident from the crack formations in the device. Therefore, high bending radius ($r$ > 16 mm) is required for sustaining acceptable device characteristics. Since the present flexible ECT can be fabricated at room temperature, low cost polymer-based substrates can be used. The strong resistance to static flexural strains observed from the present ECTs would be of great value for economically viable curved FPD devices in the future.

## Acknowledgments

This research was supported by Grant-in-Aid for JSPS Fellows (T.O., 17J01281), Scientific Research A (H.O., 17H01314) and Innovative Areas (H.O., 19H05791) from the JSPS. H.J.C. acknowledges the support from Nippon Sheet Glass Foundation for Materials Science and Engineering. H.O. acknowledges the support from the Asahi Glass Foundation and the Mitsubishi Foundation. A part of this work was supported by Dynamic Alliance for Open Innovation Bridging Human, Environment, and Materials, and by the Network Joint Research Center for Materials and Devices.

## Competing financial interests

The authors declare no competing financial interests.

## References


1) M. Kaltenbrunner, T. Sekitani, J. Reeder, T. Yokota, K. Kuribara, T. Tokuhara, M. Drack, R. Schwodiauer, I. Graz, S. Bauer-Gogonea, S. Bauer, and T. Someya, Nature **499**, 458 (2013).
2) T. Sekitani, U. Zschieschang, H. Klauk, and T. Someya, Nat Mater **9**, 1015 (2010).
3) K. Nomura, H. Ohta, A. Takagi, T. Kamiya, M. Hirano, and H. Hosono, Nature **432**, 488 (2004).
4) T. Yokota, P. Zalar, M. Kaltenbrunner, H. Jinno, N. Matsuhisa, H. Kitanosako, Y. Tachibana, W. Yukita, M. Koizumi, and T. Someya, Sci. Adv. **2**, 8 (2016).
5) S. Lee, A. Reuveny, J. Reeder, S. Lee, H. Jin, Q. Liu, T. Yokota, T. Sekitani, T. Isoyama, Y. Abe, Z. Suo, and T. Someya, Nat Nanotechnol **11**, 472 (2016).
6) H. Kimura, K. Fukuda, H. Jinno, S. Park, M. Saito, I. Osaka, K. Takimiya, S. Umezu, and T. Someya, Adv. Mater. **31**, e1808033 (2019).
7) M. Kaltenbrunner, M. S. White, E. D. Glowacki, T. Sekitani, T. Someya, N. S. Sariciftci, and S. Bauer, Nat Commun **3**, 770 (2012).
8) Pedro Barquinha, Sónia Pereira, Luís Pereira, Pawel Wojcik, Paul Grey, Rodrigo Martins, and Elvira Fortunato, Adv. Electron. Mater. **1**, (2015).
9) T. Katase, T. Onozato, M. Hirono, T. Mizuno, and H. Ohta, Sci. Rep. **6**, 25819 (2016).
10) Satyen K. Deb, Sol. Energy Mater. Sol. Cells **92**, 245 (2008).
11) Vaibhav Jain, Hank M. Yochum, Reza Montazami, and James R. Heflin, Appl. Phys. Lett. **92**, (2008).
12) Tatsuo Niwa and Osamu Takai, Thin Solid Films **518**, 1722 (2010).
13) S. G. Altendorf, J. Jeong, D. Passarello, N. B. Aetukuri, M. G. Samant, and S. S. Parkin, Adv. Mater. **28**, 5284 (2016).
14) M. Wang, S. Shen, J. Ni, N. Lu, Z. Li, H. B. Li, S. Yang, T. Chen, J. Guo, Y. Wang, H. Xiang, and P. Yu, Adv. Mater. **29**, (2017).
15) Xiang Meng, Francis Quenneville, Frédéric Venne, Eduardo Di Mauro, Dilek Işık, Martin Barbosa, Yves Drolet, Marta M. Natile, Dominic Rochefort, Francesca Soavi, and Clara Santato, J. Phys. Chem. C **119**, 21732 (2015).
16) Takaki Onozato, Yukio Nezu, Hai Jun Cho, and Hiromichi Ohta, AIP Adv. **9**, (2019).
17) P. Grey, L. Pereira, S. Pereira, P. Barquinha, I. Cunha, R. Martins, and E. Fortunato,

Adv. Electron. Mater. **2**, (2016).

18) S. Thakoor, A. Moopenn, T. Daud, and A. P. Thakoor, J. Appl. Phys. **67**, 3132 (1990).

19) P. G. Dickens and M. S. Whittingham, Quarterly Reviews, Chemical Society **22**, 30 (1968).

20) M. J. Duggan, T. Saito, and T. Niwa, Solid State Ionics **62**, 15 (1993).

21) X. H. Xia, J. P. Tu, J. Zhang, X. L. Wang, W. K. Zhang, and H. Huang, Sol. Energy Mater. Sol. Cells **92**, 628 (2008).

22) L. Pereira, D. Gaspar, D. Guerin, A. Delattre, E. Fortunato, and R. Martins, Nanotechnology **25**, 094007 (2014).

23) William D. Callister and David G. Rethwisch, *Fundamentals of Materials Science and Engineering*, 5 edition ed. (Wiley, London, 2015).

24) Cheng Peng, Zheng Jia, Henry Neilson, Teng Li, and Jun Lou, Adv. Eng. Mater. **15**, 250 (2013).

25) J. L. Ni, X. F. Zhu, Z. L. Pei, J. Gong, C. Sun, and G. P. Zhang, J. Phys. D: Appl. Phys. **42**, (2009).

26) Darran R. Cairns, Richard P. Witte, Daniel K. Sparacin, Suzanne M. Sachsman, David C. Paine, Gregory P. Crawford, and R. R. Newton, Appl. Phys. Lett. **76**, 1425 (2000).

27) Sung Kyu Park, Jeong In Han, Dae Gyu Moon, and Won Keun Kim, Jpn. J. Appl. Phys. **42**, 623 (2003).

28) D. Soo Choi, S. Ho Han, H. Kim, S. Hee Kang, Y. Kim, C. M. Yang, T. Y. Kim, D. Ho Yoon, and W. Seok Yang, Nanotechnology **25**, 395702 (2014).

29) K. Sakamoto, H. Kuwae, N. Kobayashi, A. Nobori, S. Shoji, and J. Mizuno, Sci. Rep. **8**, 2825 (2018).

30) J. Yun, Y. H. Park, T. S. Bae, S. Lee, and G. H. Lee, ACS Appl Mater Interfaces **5**, 164 (2013).

31) S. J. Lee, Y. Kim, J. Y. Hwang, J. H. Lee, S. Jung, H. Park, S. Cho, S. Nahm, W. S. Yang, H. Kim, and S. H. Han, Sci. Rep. **7**, 3131 (2017).

32) Xiaojia Zhang, Xingqiang Liu, Yupeng Zhang, Rongrong Bao, Dengfeng Peng, Tianfeng Li, Guoyun Gao, Wenxi Guo, and Caofeng Pan, J. Mater. Chem. C **4**, 8130 (2016).

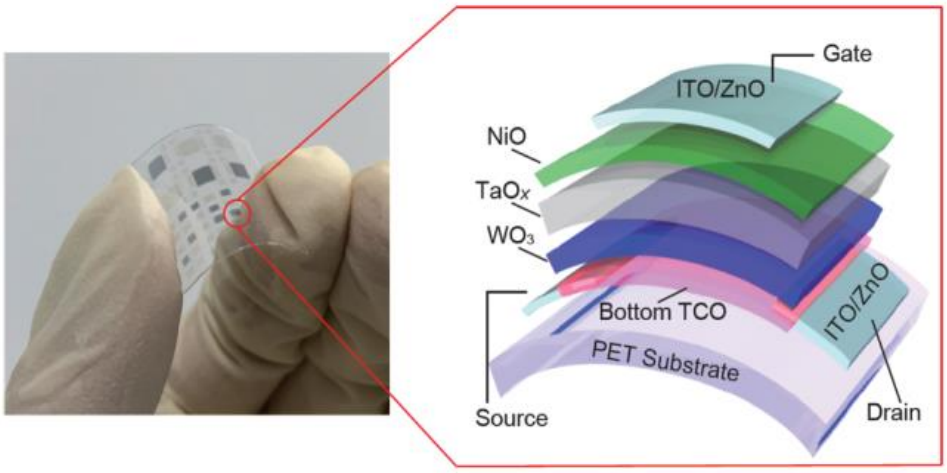


**Fig. 1.** A flexible ECT. Using the stencil masks, we fabricated an ECT on 0.1-mm-thick PET substrate. The resultant ECT is bendable.

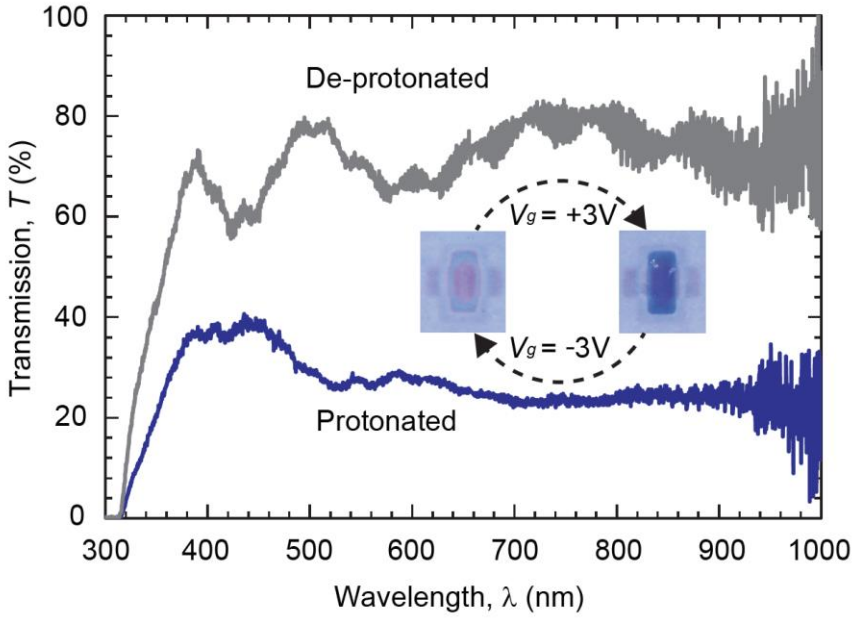


**Fig. 2.** Optical transmission spectra of the flexible ECT, which is composed of 50-nm-thick ITO, 10-nm-thick ZnO, 20-nm-thick NiO, 250-nm-thick $TaO_x$, 100-nm-thick $WO_3$, 10-nm-thick ZnO, and 0.1-mm-thick PET. The optical transmission in the visible light region dramatically decreased after the protonation and it recovered after the de-protonation. The inset shows the photographs of the device. After the protonation (applied $V_g$= +3V), the device becomes dark blue whereas the device was transparent at the de-protonation (applied $V_g$= −3V).

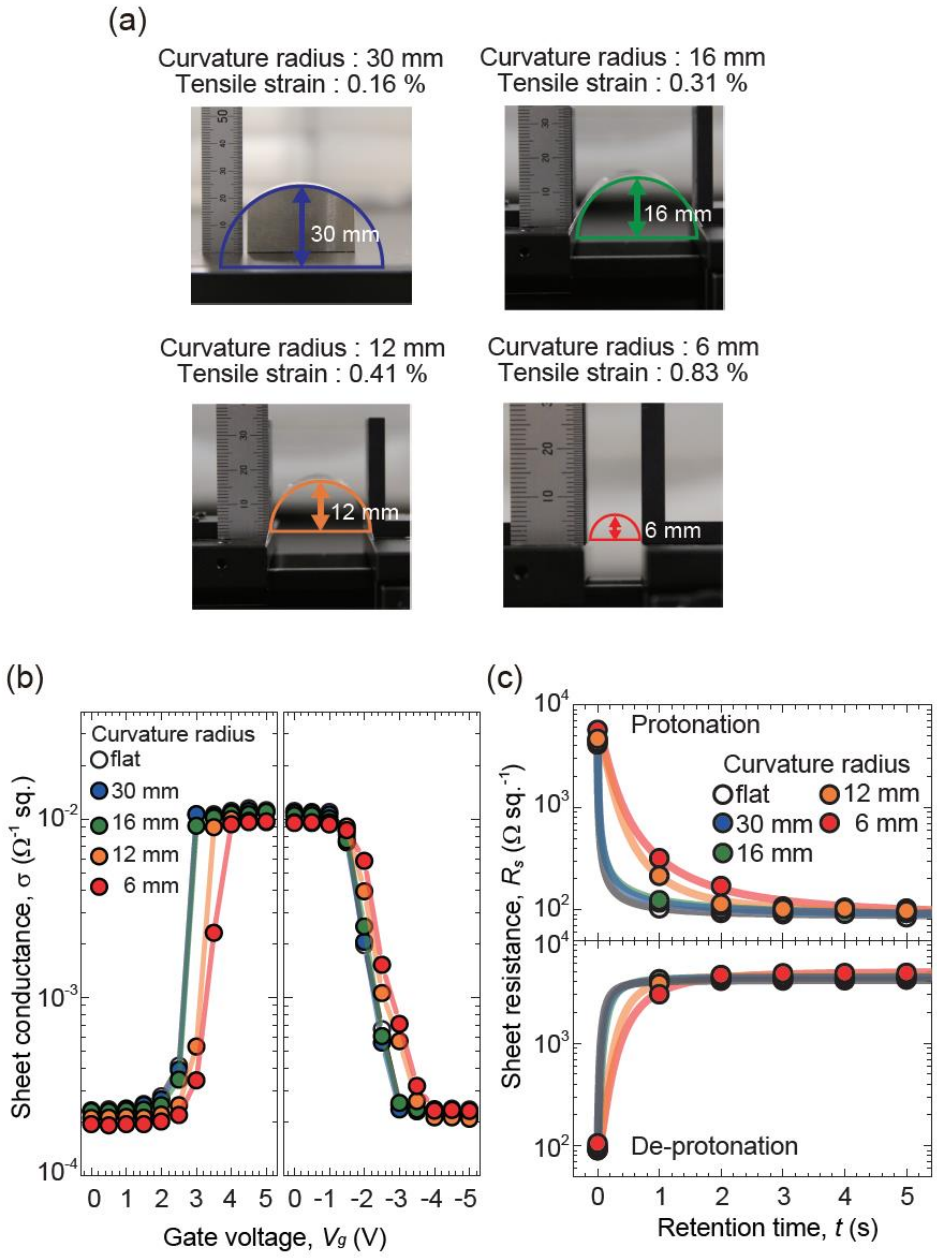


**Fig. 3.** (a) The optical micrographs of the experimental setups of the bending test of the ECT devices at various radii of curvature. The tensile strain was kept at 0.16 % for 30 mm, 0.31 % for 16 mm, 0.41 % for 12 mm, and 0.83 % for 6 mm. (b) Sheet conductance ($\sigma_s$) as a function of applied Gate voltage ($V_g$) at various curvature radius, where positive $V_g$ applied for protonation (left panel, each $V_g$ application time of 1s), and then negative $V_g$ applied for deprotonation (right panel, each $V_g$ application time of 1 s). (c) Effect of bending on the electron transport of the ECT during protonation and de-protonation. Retention time ($t$) dependence of sheet resistance ($R_s$) under application of $\pm V_g$= 3 V.

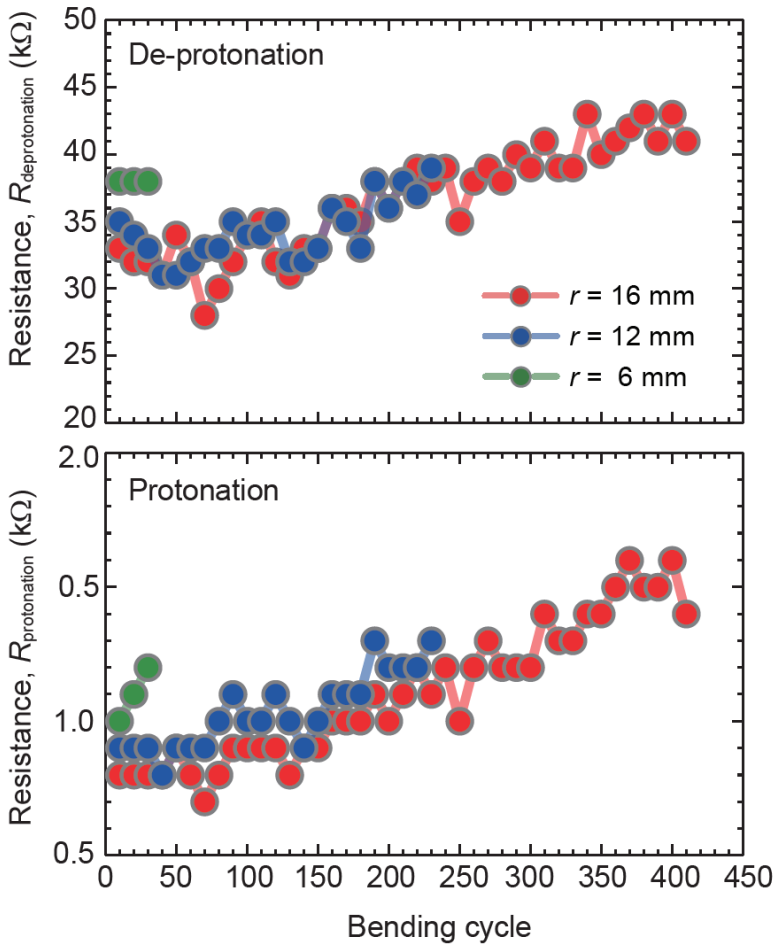


**Fig. 4.** Change in the two-terminal resistance ($R_{deprotonation}$, $R_{protonation}$) as a function of flexural cycles at the various $r$ ($r$ = 16, 12 and 6 mm). The ECT showed reasonable device characteristics even after 410 cycles of the bending test ($r$ = 16 mm).

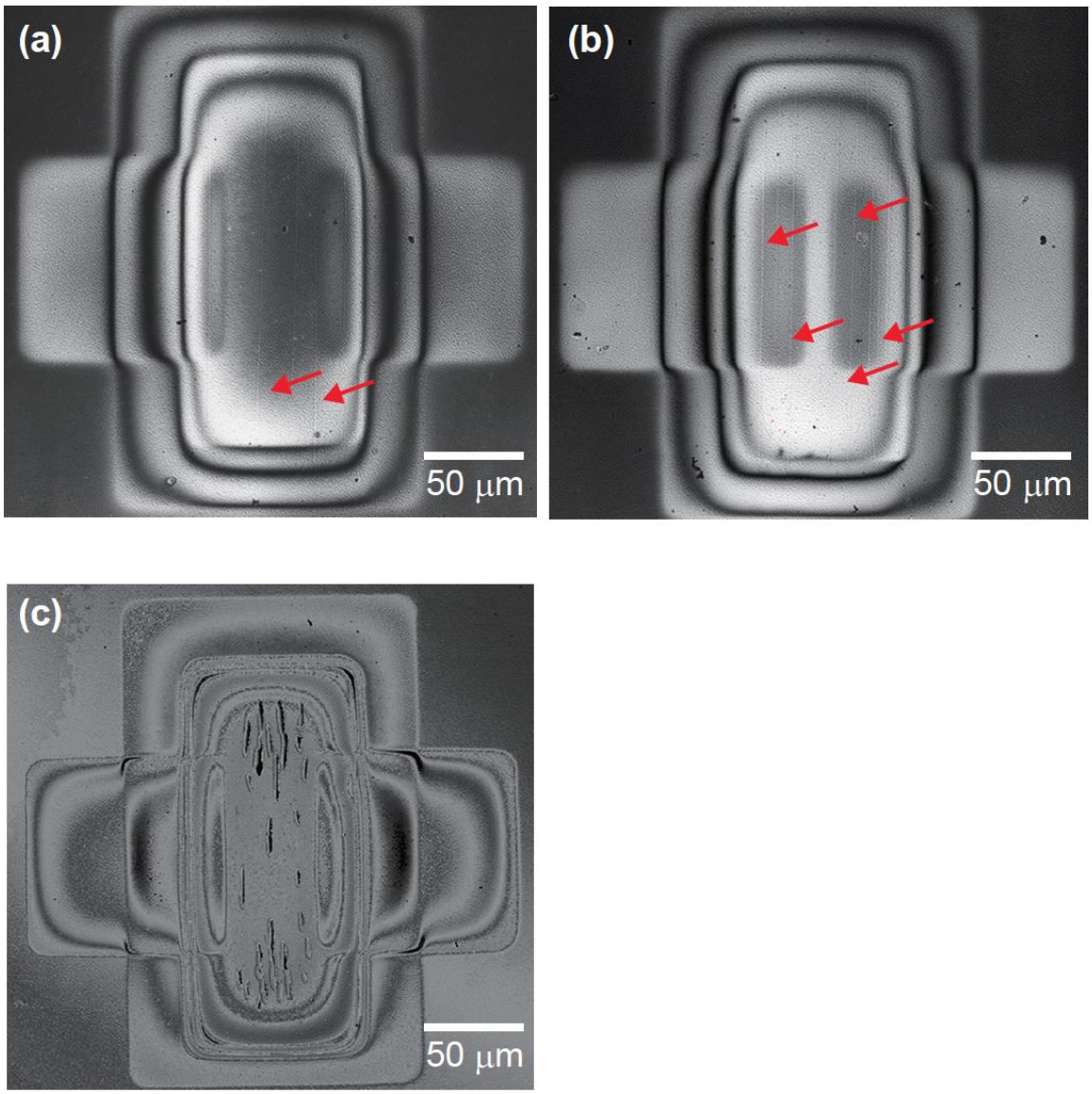


**Fig. 5.** Optical micrographs of ECTs at their fatigue limits, obtained by a laser microscope. The radii of curvature are: (a) $r$ = 16 mm, (b) $r$ = 12 mm, and (c) $r$ = 6 mm. Above, $r$ = 12 mm, the crack lines are long and straight, which are typical brittle fracture characteristics of thin amorphous films. However, at $r$ = 6 mm, clustered short elliptical pores are shown, which is likely from the fracture of porous $TaO_x$.